Journal of Non-Crystalline Solids 671 (2026) 123838

Contents lists available at ScienceDirect

Journal of Non-Crystalline Solids

journal homepage: www.elsevier.com/locate/jnoncrysol

The magnetocaloric properties of $Gd_{36}RE_{20}Ni_{20}Al_{24}$ (RE = Dy, Ho, Er) amorphous high-entropy alloys for hydrogen liquefaction application

Zhongwei Pei [a,b,1], Hangboce Yin [a,1], Songhao Shao [a], Yan Zhang [a], Meng Gao [a], Lijian Song [a], Wei Xu [a], Yu Tong [a], Xiao Jin [a], Jun Xu [a], Mingliang Xiang [a,*], Jun-Qiang Wang [a,*], Juntao Huo [a,*]

[a] CAS Key Laboratory of Magnetic Materials and Devices, and Zhejiang Key Laboratory of Magnetic Materials and Applications, Ningbo Institute of Materials Technology and Engineering, Chinese Academy of Sciences, Ningbo 315201, China
[b] School of Materials Science and Chemical Engineering, Ningbo University, Ningbo, 315211, China

ARTICLE INFO

Keywords:
Magnetocaloric effect
Amorphous high-entropy alloy
Ribbon
Spin-glass state

ABSTRACT

Amorphous high-entropy alloys (HEAs) with rare-earth elements offer great potential for low-temperature magnetic refrigeration. In this study, $Gd_{36}RE_{20}Ni_{20}Al_{24}$ (RE = Dy, Ho, Er) amorphous HEAs were systematically investigated. The alloys exhibit fully amorphous structures and spin-glass states, with Curie temperatures tunable from 40 to 50 K, proportional to the de Gennes factor of the substituted rare-earth element. Magnetic measurements reveal relatively large magnetocaloric properties, with peak value of magnetic entropy changes of 7.79, 8.75, and 8.55 J kg^{-1} K^{-1} for RE = Dy, Ho, and Er, respectively, under a magnetic field change of 5 T. The corresponding refrigerant capacities reach 470, 528, and 492 J kg^{-1}. The broad working temperature spans are attributed to the atomic disorder, chemical disorder, and spin-glass state of these alloys. These results demonstrate that the designed rare-earth-containing amorphous HEAs are promising candidates for magnetic refrigerants in the 20–77 K range, particularly for hydrogen liquefaction applications.

1. Introduction

Magnetic refrigeration (MR) based on the magnetocaloric effect (MCE) has emerged as a promising, eco-friendly, and energy-efficient alternative to conventional vapor-compression refrigeration systems [1–5]. The MCE performance of a refrigerant is primarily evaluated by the magnetic entropy change ($|\Delta S_M|$), which originates from the field-induced reversible transition of magnetic moments between ordered and disordered states upon the application and removal of an external magnetic field [6]. Recently, magnetocaloric materials working in the temperature range required by hydrogen liquefaction, i.e., 20–77 K, have attracted increasing attention, especially when pre-cooled by liquid nitrogen [7–9]. This growing interest can be attributed to two main reasons: (i) hydrogen liquefaction is an efficient method for the storage and transportation of hydrogen energy [3,10,11]; (ii) magnetic refrigeration offers high efficiency, which can significantly reduce electricity consumption.

Due to the use of non-magnetic constituent elements like Al or Cu, which tend to isolate magnetic atoms in the alloy structure, rare-earth (RE) based amorphous alloys generally work at low temperatures as magnetocaloric materials [12–17]. This makes them promising candidates for magnetocaloric applications in the temperature range required by hydrogen liquefaction. In addition, the Curie temperatures (T_C) of RE based amorphous alloys can be effectively tuned by changing the constituent elements [18–21].

Amorphous high-entropy alloys (HEAs), developed using the compositional design principles of HEAs, have emerged as a rapidly expanding research focus in the field of magnetocaloric amorphous alloys [5,19,22,23]. These alloys integrate the distinctive attributes of both HEAs and amorphous alloys, such as pronounced topological and chemical disorder, endowing them with unique characteristics and markedly enhanced properties [12,24]. In the magnetocaloric field, these alloys, owing to their second-order phase transition characteristics, exhibit negligible magnetic and thermal hysteresis.

In our previous work, we developed a first-generatuion series of equiatomic $Gd_{20}Tb_{20}Dy_{20}Al_{20}M_{20}$ (M = Fe, Co and Ni) amorphous

* Corresponding authors.
E-mail addresses: xiangmingliang@nimte.ac.cn (M. Xiang), jqwang@nimte.ac.cn (J.-Q. Wang), huojuntao@nimte.ac.cn (J. Huo).
[1] Zhongwei Pei and Hangboce Yin have contributed equally to this work.

https://doi.org/10.1016/j.jnoncrysol.2025.123838
Received 19 August 2025; Received in revised form 23 October 2025; Accepted 23 October 2025

HEAs. These alloys exhibited T_C of 112 K for M = Fe, 58 K for M = Co, and 45 K for M = Ni, and peak value of magnetic entropy change ($|\Delta S_M^{pk}|$) of 5.96, 9.43, and 7.25 J kg^{-1} K^{-1}, respectively, under a magnetic field change ($\mu_0\Delta H$) of 5 T [12]. Furthermore, the compositional design was advanced to develop a second-generation non-equiatomic amorphous HEAs, namely $Gd_{36}Tb_{20}Co_{20}Al_{24}$, which exhibited a T_C and a $|\Delta S_M^{pk}|$ of 81 K and 9 J kg^{-1}(5 T) [23]. The results indicate that Ni addition effectively reduces the T_C of the RE-containing amorphous HEA while maintaining its relatively large magnetocaloric performance. In addition, the second-generation amorphous HEAs not only expand the compositional space but also provide the potential to overcome the performance limitations of first-generation amorphous HEAs [5].

To address the refrigeration requirements in the temperature range required by hydrogen liquefaction, we adopted a compositional design strategy by incorporating Ni into $Gd_{36}Tb_{20}Co_{20}Al_{24}$. Additionally, to enhance the MCE performance, we replaced Tb in the composition with elements possessing a large magnetic moment, namely Dy, Ho, and Er [25]. Amorphous $Gd_{36}RE_{20}Ni_{20}Al_{24}$ (RE = Dy, Ho, Er) HEAs were prepared by the melt-spinning technique, and the effects of different RE elements on their magnetic behavior and magnetocaloric properties were systematically investigated.

2. Experimental details

Master alloys with the nominal compositions $Gd_{36}RE_{20}Ni_{20}Al_{24}$ (RE = Dy, Ho, Er) were prepared by arc melting the mixtures of commercial-grade metals with purities above 99.9 wt. %. The fabrication was carried out under a Ti-gettered argon atmosphere. Each alloy ingot was remelted five times to ensure compositional homogeneity. After arc melting, the mass loss of each ingot was <0.5 %. The ingots were subsequently remelted and dropped onto a spinning copper roller with a surface velocity of 45 m s^{-1} to produce alloy ribbons. The structure of the ribbons was preliminarily examined by an X-ray diffraction (XRD, Bruker D8 Advance) over the 2θ range of 20° to 80° at a scanning rate of 6° min^{-1}. Thermal analysis of the ribbons was conducted using differential scanning calorimetry (DSC, Netzsch DSC-404-C) from room temperature to 1050 K at a heating rate of 40 K min^{-1}. Transmission electron microscopy (TEM, Thermo Fisher Talos F200x) equipped with energy-dispersive X-ray spectroscopy (EDS) was employed to investigate the nanoscale microstructure of the ribbons. The magnetic and magnetocaloric properties were measured using a Physical Property Measurement System (PPMS, Quantum Design DynaCool). The direction of the applied magnetic field is parallel to the long axis of the ribbons. The field-cooled (FC) and zero-field-cooled (ZFC) magnetization-temperature (M-T) curves were measured under an applied magnetic field of 0.02 T. The isothermal magnetization (M-μ_0H) curves were recorded in the field range of 0 to 5 T. Magnetic hysteresis loops and AC susceptibility curves of the studied ribbons were measured with a Magnetic Property Measurement System (MPMS, Quantum Design SQUID-VSM). The AC susceptibility measurements were carried out under a field of 2 Oe.

3. Results and discussion

Fig. 1(a) and (b) present the XRD patterns and DSC curves of $Gd_{36}RE_{20}Ni_{20}Al_{24}$ (RE = Dy, Ho, Er) alloys, respectively. Fig. 1(a) shows the broad and diffuse peaks of $Gd_{36}RE_{20}Ni_{20}Al_{24}$ (RE = Dy, Ho, Er) alloys, indicating the fully amorphous structure of these alloys. All DSC curves for these alloys exhibit a distinct endothermic peak corresponding to the glass transition, followed by sharp exothermic peaks associated with crystallization. These thermal events confirm the amorphous nature of these alloys. The glass transition temperature (T_g), crystallization temperature (T_x), and liquidus temperature (T_l) are marked in Fig. 1(b) and summarized in Table 1. The criteria for evaluating glass-forming ability (GFA), namely the reduced glass transition temperature (T_{rg}) and the γ parameter, were calculated using the following expressions: $T_{rg} = T_g/T_l$ [26,27], and $\gamma = T_x/(T_g+T_l)$ [28]. The width of supercooled liquid region (ΔT_x) was calculated as $\Delta T_x = T_x$-T_g [25,29,30], which reflects the resistance to crystallization in amorphous alloys. Table 1 lists the T_{rg}, γ, and ΔT_x values of $Gd_{36}RE_{20}Ni_{20}Al_{24}$ (RE = Dy, Ho, Er) alloys. All the studied alloys exhibit relatively high T_{rg}, γ, and ΔT_x values, indicating high GFA and thermal stability.

The microstructure of $Gd_{36}RE_{20}Ni_{20}Al_{24}$ (RE = Dy, Ho, Er) alloys was examined using high-resolution TEM (HR-TEM) and selected area electron diffraction (SAED), as shown in Fig. 2. All the studied alloys exhibit maze-like patterns in the HR-TEM images. The SAED patterns in the insets of Fig. 2(a–c) show typical diffuse halo rings without any discernible diffraction spots. These results confirm that $Gd_{36}RE_{20}Ni_{20}Al_{24}$ (RE = Dy, Ho, Er) alloys possess a fully amorphous structure [23,31], consistent with the findings from their XRD and DSC analyses. Fig. 3 displays the high-angle-annular-dark-field (HAADF) images and EDS mapping results of the $Gd_{36}RE_{20}Ni_{20}Al_{24}$ (RE = Dy, Ho, Er) alloys, in which all elements are homogeneously distributed.

Fig. 4 presents the FC and ZFC M-T curves of $Gd_{36}RE_{20}Ni_{20}Al_{24}$ (RE = Dy, Ho, Er) alloys. Based on the FC M-T curves, the dM/dT-T curves of the studied alloys were calculated and are shown in the insets of Fig. 4. The T_C of $Gd_{36}RE_{20}Ni_{20}Al_{24}$ (RE = Dy, Ho, Er) alloys is determined to be 50, 45, and 40 K, respectively, corresponding to the minima of the dM/dT-T curves. The T_C of RE-based alloys is proportional to the de-Gennes factor of the RE elements [32,33]. The theoretically calculated de Gennes factor values of Dy, Ho, and Er are 7.1, 4.5, and 2.5, respectively. This is consistent with the experimental results showing that the T_C of the alloy system decreases gradually as the RE element changes from Dy

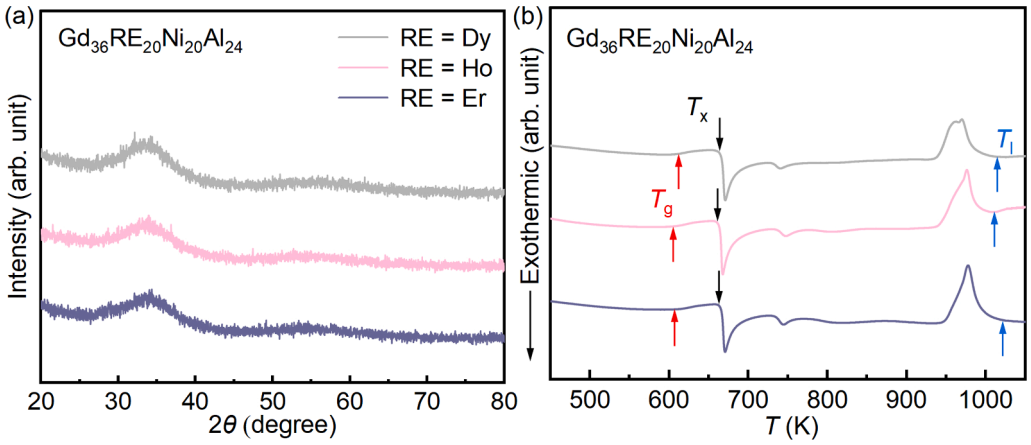

Fig. 1. (a) XRD and (b) DSC curves of $Gd_{36}RE_{20}Ni_{20}Al_{24}$ (RE = Dy, Ho, Er) alloys.

Table 1
The glass transition temperature (T_g), crystallization temperature (T_x), liquidus temperature (T_l), width of supercooled liquid region (ΔT_x), reduced glass transition temperature (T_{rg}), parameter γ, Curie temperature (T_C), peak value of magnetic entropy change ($|\Delta S_M^{pk}|$), full-width at half-maximum of the $|\Delta S_M|$-T curve (ΔT_{FWHM}), refrigeration capacity (RC), and relative cooling power (RCP) for $Gd_{36}RE_{20}Ni_{20}Al_{24}$ (RE = Dy, Ho, Er) alloys, together with other amorphous HEAs reported recently. The "-" symbol in the table denotes data not reported in the literature.

Sample	T_g (K)	T_x (K)	T_l (K)	ΔT_x (K)	T_{rg}	γ	T_C (K)	$\lvert\Delta S_M^{pk}\rvert$ (J kg^{-1} K^{-1}, 5 T)	ΔT_{FWHM} (K, 5 T)	RC (J kg^{-1}, 5 T)	RCP (J kg^{-1}, 5 T)	Ref.
$Gd_{36}Dy_{20}Ni_{20}Al_{24}$	612	664	1021	52	0.599	0.407	50	7.79	75.4	470	588	This work
$Gd_{36}Ho_{20}Ni_{20}Al_{24}$	605	661	1011	56	0.598	0.409	45	8.75	74.8	528	655	This work
$Gd_{36}Er_{20}Ni_{20}Al_{24}$	607	663	1015	56	0.598	0.409	40	8.55	71.4	492	611	This work
$Gd_{36}Tb_{20}Co_{20}Al_{24}$	586	638	1064	52	0.551	0.386	81	8.9	72.0	499	641	[23]
$Dy_{36}Tb_{20}Co_{20}Al_{24}$	628	674	1078	46	0.583	0.395	40	8.2	50.5	300	415	[23]
$Gd_{25}Tb_{25}Co_{25}Al_{25}$	612	659	–	47	–	–	73	8.88	65	–	577	[25]
$Gd_{25}Dy_{25}Co_{25}Al_{25}$	627	669	–	42	–	–	60	8.72	65	–	567	[25]
$Gd_{20}Tb_{20}Dy_{20}Ni_{20}Al_{20}$	582	607	–	25	–	–	45	7.25	70	507	–	[12]
$Gd_{20}Tb_{20}Dy_{20}Fe_{20}Al_{20}$	575	604	–	29	–	–	112	5.96	116	691	–	[12]
$Gd_{10}Tb_{10}Dy_{10}Ho_{10}Er_{10}$ -$Y_{10}Ni_{10}Co_{10}Ag_{10}Al_{10}$	597	636	–	39	–	–	24	10.64	50	532	–	[44]

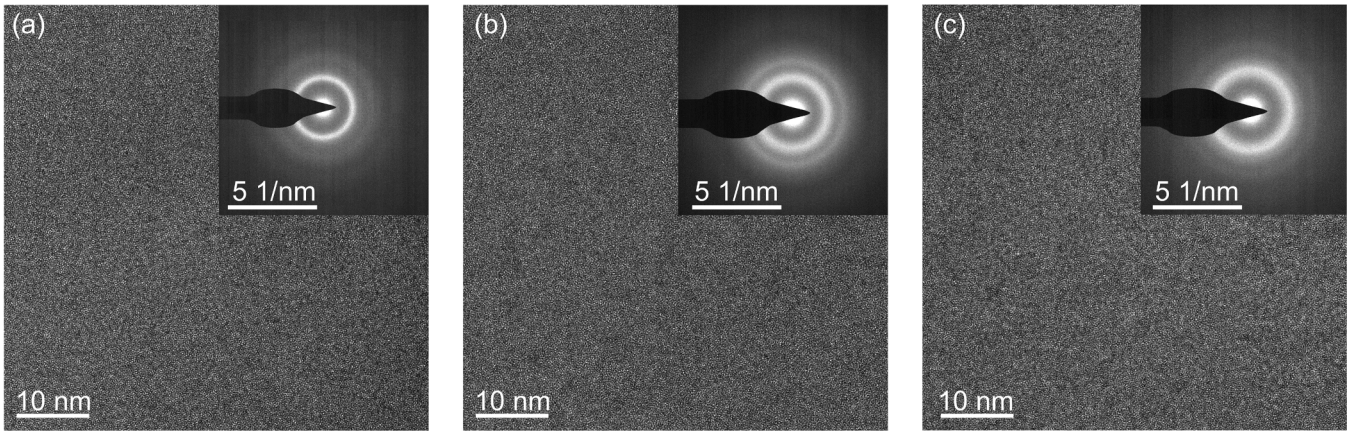

Fig. 2. The HR-TEM images and corresponding SAED patterns, insets, of $Gd_{36}RE_{20}Ni_{20}Al_{24}$ alloys with RE = (a) Dy, (b) Ho, and (c) Er.

to Er. Each sample exhibits a peak in its ZFC curve, with the corresponding peak temperatures (T_p) for $Gd_{36}RE_{20}Ni_{20}Al_{24}$ (RE = Dy, Ho, and Er) alloys being 37, 28, and 26 K, respectively. The FC and ZFC M-T curves of the studied alloys exhibit a distinct divergence at low temperatures, suggesting the possible presence of spin-glass (SG) behavior [34,35]. To identify the SG state of the alloys, the hysteresis loops of all the studied alloys were measured, as shown in Fig. 5(a–c). The coercivity derived from the hysteresis loops is presented in Fig. 5(d). The results show that the coercivity of all studied alloys at T_p is much smaller than the external magnetic field applied during the ZFC measurements (0.02 T), indicating that all alloys exhibit a SG state. In addition, the SG state of the studied alloys was confirmed by comparing the results of the AC susceptibility analysis with the typical values of canonical SG. The AC susceptibility curves are shown in the insets of Fig. 6. As the system approaches the transition point, the dynamics slow down, causing the relaxation time ($\tau_{max} = \frac{1}{\omega}$) to exhibit a power-law behavior [36]:

$$\tau_{max} = \tau_0 \times \left(\frac{T_p}{T_s} - 1\right)^{-z\nu} \quad (1)$$

where ω represents the frequency, τ_0 is related to the relaxation time of individual atomic magnetic moment, T_s represents the ideal freezing temperature, $z\nu$ represents the critical exponent. For canonical spin glasses, τ_0 and $z\nu$ are typically in the ranges of $\sim 10^{-10}$–10^{-13} and 4–13, respectively [25,36]. By applying the above equation to fit the experimental data, the results shown in Fig. 6(a–c) give $\tau_0 = \sim 10^{-12}$ s, $T_s =$ 39.3 K, and $z\nu = 11.6$ for RE = Dy; $\tau_0 = \sim 10^{-13}$ s, $T_s = 36.2$ K, and $z\nu =$ 7.6 for RE = Ho; $\tau_0 = \sim 10^{-11}$ s, $T_s = 31.4$ K, and $z\nu = 5.9$ for RE = Er. These results agree well with the typical values reported for SGs, thereby confirming that the studied alloys exhibit a SG state. For alloys containing RE elements, e.g., Dy, Ho and Er, strong random magnetic anisotropy (RMA) disrupts the long-range ferromagnetic order. At low temperatures, the spins tend to align rigidly with their local anisotropy axes, resulting in complicated ground states characterized by randomly oriented magnetic moments and pronounced magnetic irreversibility [37–39]. The strong RMA leads to the SG behavior of the studied alloys [25].

To evaluate the magnetocaloric properties, M-$\mu_0 H$ curves of $Gd_{36}RE_{20}Ni_{20}Al_{24}$ (RE = Dy, Ho, Er) alloys were measured and are plotted in Fig. 7(a-c), respectively. At temperatures below T_C, the magnetization for each alloy increases abruptly with increasing applied magnetic field and then increases slowly, indicating ferromagnetic behavior. In contrast, the magnetization curves exhibit a linear dependence on the applied magnetic field at temperatures above T_C, confirming the paramagnetic state. This indicates a ferromagnetic-to-paramagnetic transition in all studied alloys with increasing temperature. It is noteworthy that the M-$\mu_0 H$ curves of all the studied alloys do not reach saturation under the maximum applied field of 5 T. The Dy-, Ho- and Er-containing amorphous ribbons prepared by Xue et al. [25] and Jia et al. [20] show spin glass behavior at low temperatures. The above results indicate that the magnetization of the alloys does not reach saturation even under an applied field of 5 T. This indicates that a higher external magnetic field is required to overcome the effect of RMA in the alloys. Since the studied alloys ($Gd_{36}RE_{20}Ni_{20}Al_{24}$, RE = Dy, Ho, Er) possess compositions similar to the aforementioned systems, the strong RMA effect accounts for their failure to reach magnetic saturation even

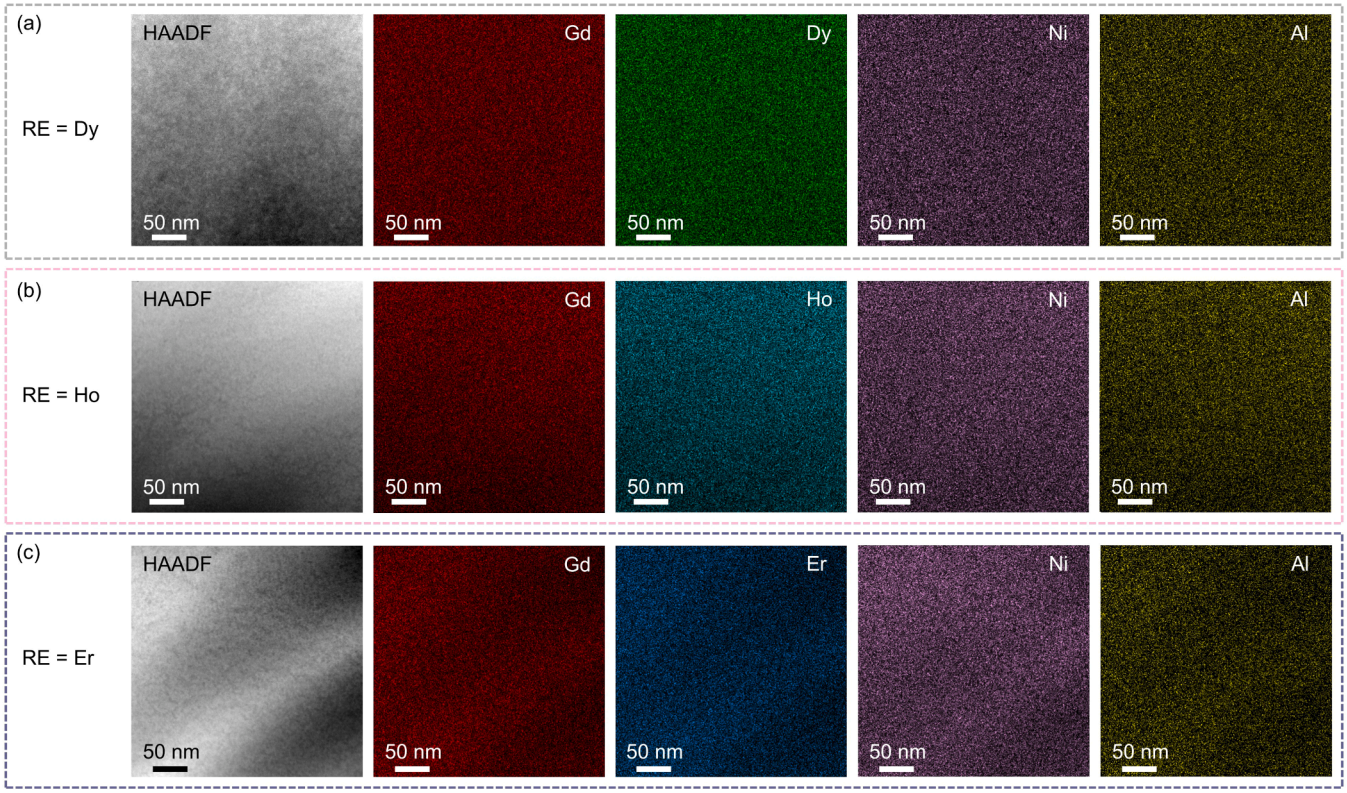

Fig. 3. HAADF images and EDS mapping results of $Gd_{36}RE_{20}Ni_{20}Al_{24}$ alloys with RE = (a) Dy, (b) Ho, and (c) Er, respectively.

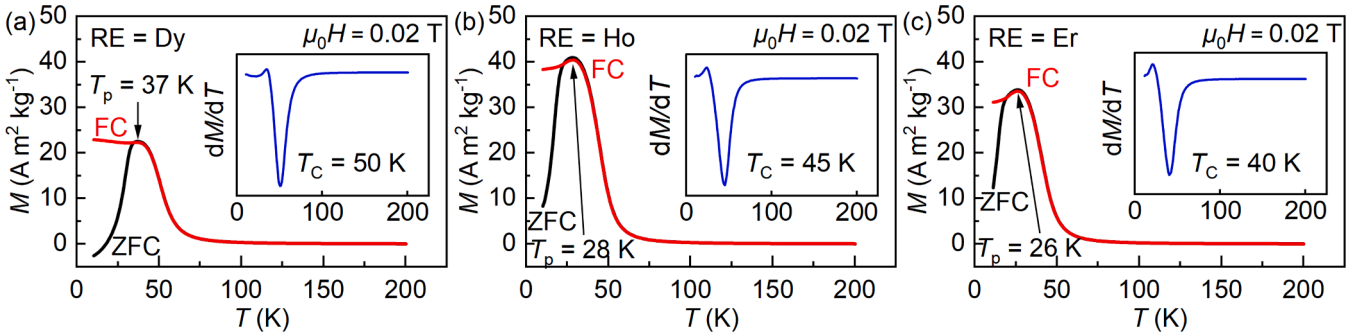

Fig. 4. ZFC and FC *M-T* curves of $Gd_{36}RE_{20}Ni_{20}Al_{24}$ alloys with RE = (a) Dy, (b) Ho, and (c) Er under a magnetic field of 0.02 T The insets show the d*M*/d*T*-*T* curves.

under an applied field of 5 T. The intersections of the M-μ_0H curves at 10 K and 20 K for $Gd_{36}Dy_{20}Ni_{20}Al_{24}$, and at 5 K and 10 K for $Gd_{36}Er_{20}Ni_{20}Al_{24}$, are attributed to SG behavior, consistent with observations in previous reports [25,34].

Fig. 8 shows the Arrott plots for $Gd_{36}RE_{20}Ni_{20}Al_{24}$ (RE = Dy, Ho, Er) alloys. The inset of Fig. 8(a) presents the magnified plots at 10, 20, and 30 K for $Gd_{36}Dy_{20}Ni_{20}Al_{24}$ alloy. According to the Banerjee criterion [40], a negative slope in the Arrott plot indicates a first-order magnetic transition (FOMT), whereas a positive slope corresponds to a second-order magnetic transition (SOMT). The $Gd_{36}Dy_{20}Ni_{20}Al_{24}$ alloy exhibits a negative slope at low temperatures, as shown in the inset of Fig. 8(a), confirming the presence of the FOMT. In contrast, the positive slopes in the Arrott plots for $Gd_{36}Ho_{20}Ni_{20}Al_{24}$ and $Gd_{36}Ho_{20}Ni_{20}Al_{24}$ alloys indicate SOMT characteristics. Given the limitations of the Arrott plot results [41], additional methods were employed to further clarify the magnetic transition types in $Gd_{36}RE_{20}Ni_{20}Al_{24}$ (RE = Dy, Ho, Er) alloys. The corresponding results are presented below.

Fig. 9 displays the temperature dependence of $|\Delta S_M|$ under various $\mu_0\Delta H$ for $Gd_{36}RE_{20}Ni_{20}Al_{24}$ (RE = Dy, Ho, Er) alloys. According to the Maxwell relation, ΔS_M of magnetic materials can be calculated from the isothermal M-μ_0H curves using the integral method [42]:

$$\Delta S_M = \mu_0 \int_0^{H_{max}} (\partial M/\partial T)\mathrm{d}H = \mu_0 \left(\int_0^{H} M(T_i, H)\mathrm{d}H - \int_0^{H} M(T_{i+1}, H)\mathrm{d}H \right) \Big/ (T_i - T_{i+1}) \quad (2)$$

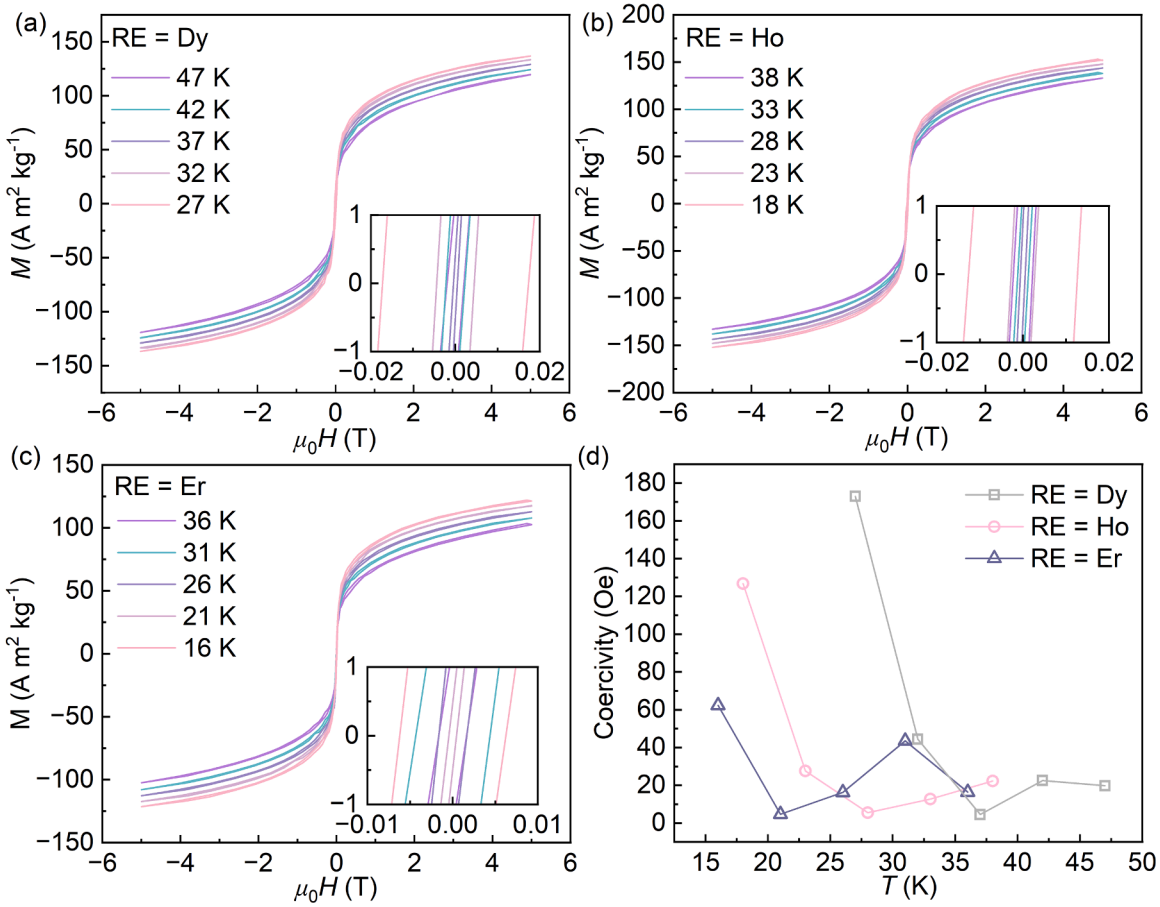

Fig. 5. Magnetic hysteresis loops of $Gd_{36}RE_{20}Ni_{20}Al_{24}$ alloys with RE = (a) Dy, (b) Ho, and (c) Er. The inset shows the magnified image. (d) The coercivity of all studied alloys.

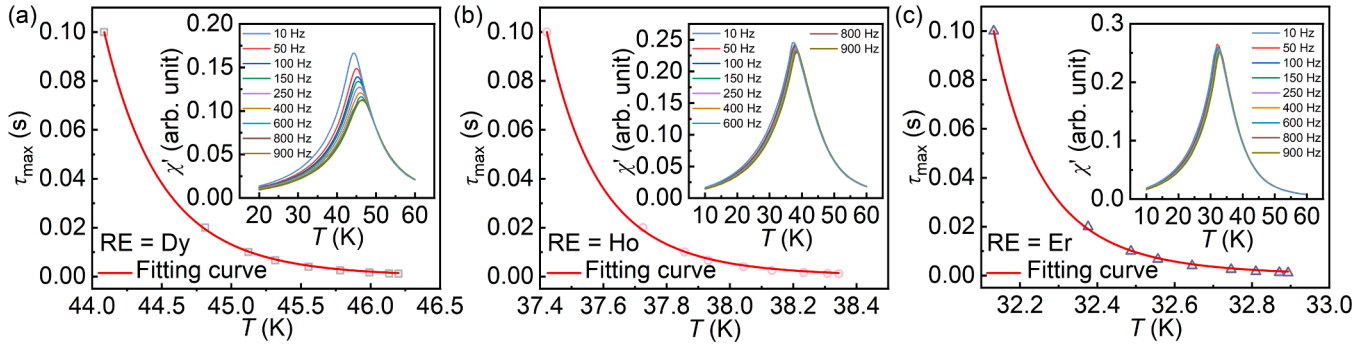

Fig. 6. τ_{max}-T curves for of $Gd_{36}RE_{20}Ni_{20}Al_{24}$ alloys with RE = (a) Dy, (b) Ho, and (c) Er. The insets are the AC susceptibility curves at frequencies ranging from 10 to 900 Hz.

where $\mu_0 H_{max}$ represents the maximum value of the applied magnetic field. For each alloy, $|\Delta S_M|$ increases with the applied magnetic field over entire temperature range. As shown in Fig. 9(a-c), the $|\Delta S_M^{pk}|$ reaches 7.79, 8.85, and 8.55 J kg^{-1} K^{-1} for $Gd_{36}RE_{20}Ni_{20}Al_{24}$ (RE = Dy, Ho, Er) alloys, respectively, at $\mu_0\Delta H$ = 5 T, demonstrating that RE substitution significantly influences the ΔS_M values of the alloys. In addition, all $|\Delta S_M|$-T curves exhibit working temperature ranges covering the temperature range of 20–77 K. This indicates the success of our compositional design for amorphous HEAs working in the temperature range required by hydrogen liquefaction.

In addition to ΔS_M, two other key parameters for evaluating the MCE properties are the relative cooling power (*RCP*) and the refrigeration capacity (*RC*). These serve as indirect indicators of the heat that can be transferred in an idealized refrigeration process and can be estimated as follows [18,43]:

$$RCP = \left|\Delta S_M^{pk}\right| \times \Delta T_{FWHM} = \left|\Delta S_M^{pk}\right| \left(T_2 - T_1\right) \quad (3)$$

$$RC = \int_{T_1}^{T_2} |\Delta S_M(T)| dT \quad (4)$$

where T_1 and T_2 are the lower and upper temperatures at the full-width at half-maximum of the $|\Delta S_M|$-T curve (ΔT_{FWHM}), which is taken as the working temperature span. Table 1 summarizes the magnetocaloric parameters for $Gd_{36}RE_{20}Ni_{20}Al_{24}$ (RE = Dy, Ho, Er) alloys and several

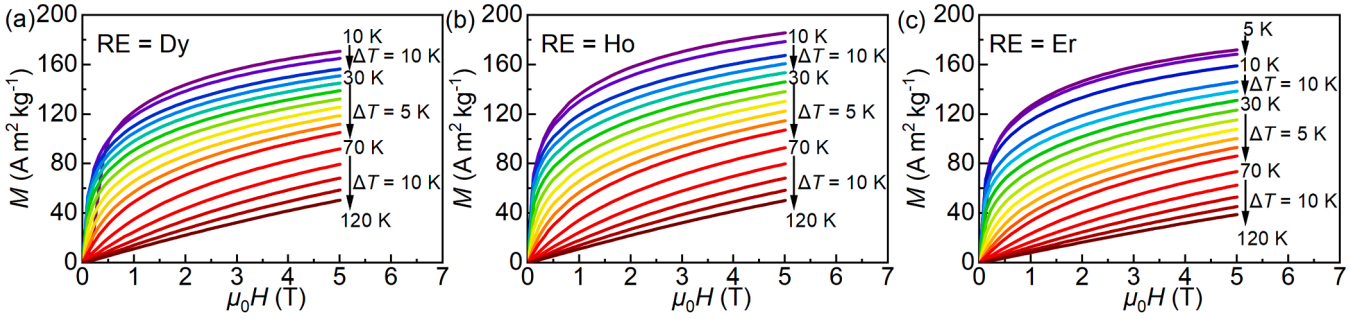

Fig. 7. Isothermal M-$\mu_0 H$ curves of $Gd_{36}RE_{20}Ni_{20}Al_{24}$ alloys with RE = (a) Dy, (b) Ho, and (c) Er measured in the field range of 0–5 T.

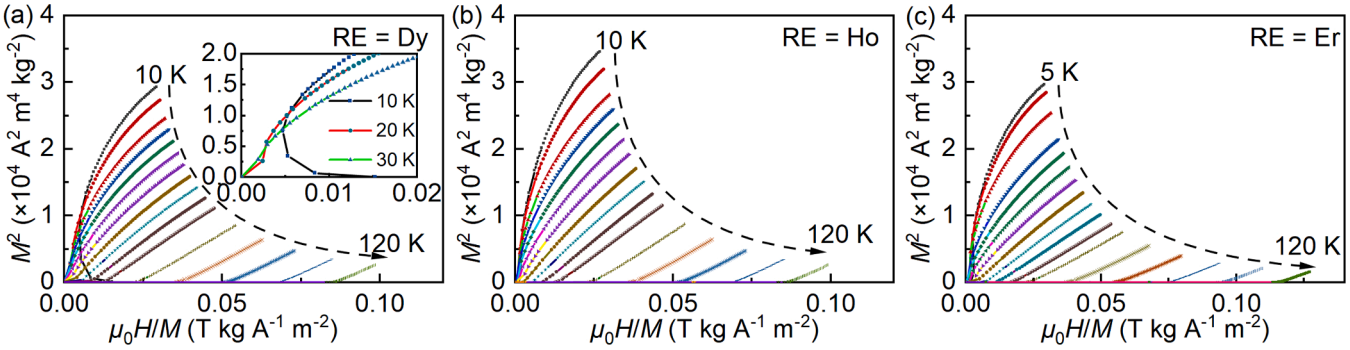

Fig. 8. Arrott plots of $Gd_{36}RE_{20}Ni_{20}Al_{24}$ alloys with RE = (a) Dy, (b) Ho, and (c) Er. The inset in (a) shows an enlarged view at 10 K, 20 K, and 30 K.

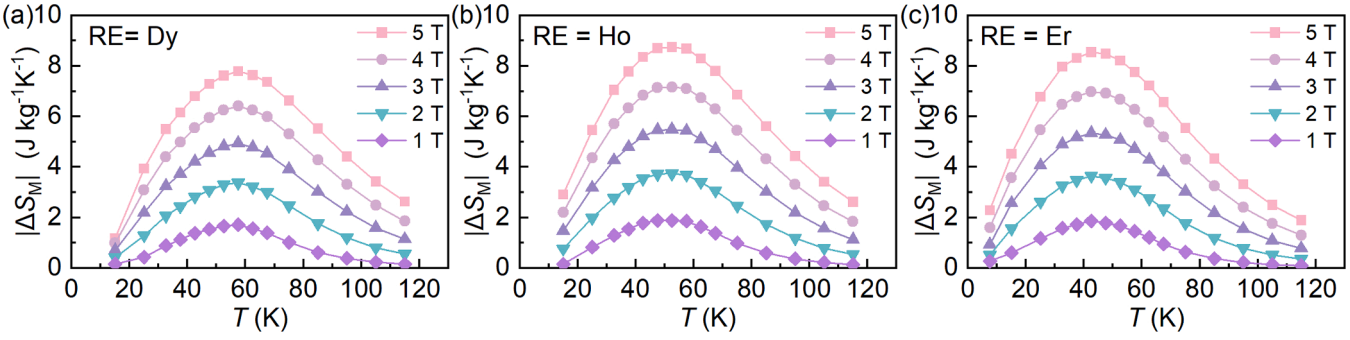

Fig. 9. $|\Delta S_M|$-T curves of $Gd_{36}RE_{20}Ni_{20}Al_{24}$ alloys with RE = (a) Dy, (b) Ho, and (c) Er.

representative amorphous HEAs. The $Gd_{36}RE_{20}Ni_{20}Al_{24}$ (RE = Dy, Ho, Er) alloys exhibit the relatively high magnetocaloric performance. Among these alloys, $Gd_{36}Ho_{20}Ni_{20}Al_{24}$ shows the largest $|\Delta S_M^{pk}|$ and RC values. All the studied alloys possess a wide ΔT_{FWHM}. In the SG state, the magnetic moments become locked into equilibrium orientations without establishing long-range magnetic order. Unlike in a ferromagnetic state, these frozen spins are more resistant to rotation, which suppresses spin dynamics [44,45]. As a result, the existence of a spin-glass state can effectively broaden the working temperature span of magnetocaloric materials. Therefore, the wide ΔT_{FWHM} of all studied alloys is attributed to their disordered atomic structure, chemical disorder, and SG state. The cocktail effect in HEAs significantly influences their properties through interactions among different elements [46]. Notably, the magnetic properties, e.g., T_C, $|\Delta S_M^{pk}|$, RCP and RC, of $Gd_{36}RE_{20}Ni_{20}Al_{24}$ (RE = Dy, Ho, Er) amorphous HEAs can be gradually tuned by substituting different RE elements, as summarized in Table 1, highlighting the presence of the cocktail effect in these alloys.

The universal curve is widely used for analyzing the magnetic transition type of MCE materials [47,48]. The y-axis of the universal curves is obtained from the $|\Delta S_M|$-T curves by normalizing ΔS_M to its peak value, ΔS_M^{pk}. The temperature axis of the magnetocaloric curves is normalized into a dimensionless form (θ) using either one or two reference temperatures, which serves as the x-axis of the universal curves, according to the following equations [49]:

$$\theta(1\ \text{ref}) = (T - T_{peak})/(T_r - T_{peak}) \tag{5}$$

$$\theta(2\,\text{refs}) = \begin{cases} -(T - T_{peak})/(T_{r1} - T_{peak}); T \text{ and } T_{r1} \le T_{peak} \\ (T - T_{peak})/(T_{r2} - T_{peak}); T \text{ and } T_{r2} > T_{peak} \end{cases} \tag{6}$$

where T_{peak} represents the temperature corresponding to $|\Delta S_M^{pk}|$, and T_r, T_{r1} and T_{r2} are the reference temperatures at which $\Delta S_M(T_{r1}) = \Delta S_M(T_{r2}) = 0.7\Delta S_M^{pk}$ Fig. 10(a-c) present the universal curves of $Gd_{36}RE_{20}Ni_{20}Al_{24}$ (RE = Dy, Ho, Er) alloys at $\mu_0\Delta H$ = 2–5 T using one reference temperature, while Fig. 10(d-f) show the corresponding universal curves constructed with two reference temperatures. Except for the two-reference-temperature universal curves of $Gd_{36}RE_{20}Ni_{20}Al_{24}$ (RE = Ho, Er) alloys and the one-reference-temperature universal curve of $Gd_{36}Er_{20}Ni_{20}Al_{24}$

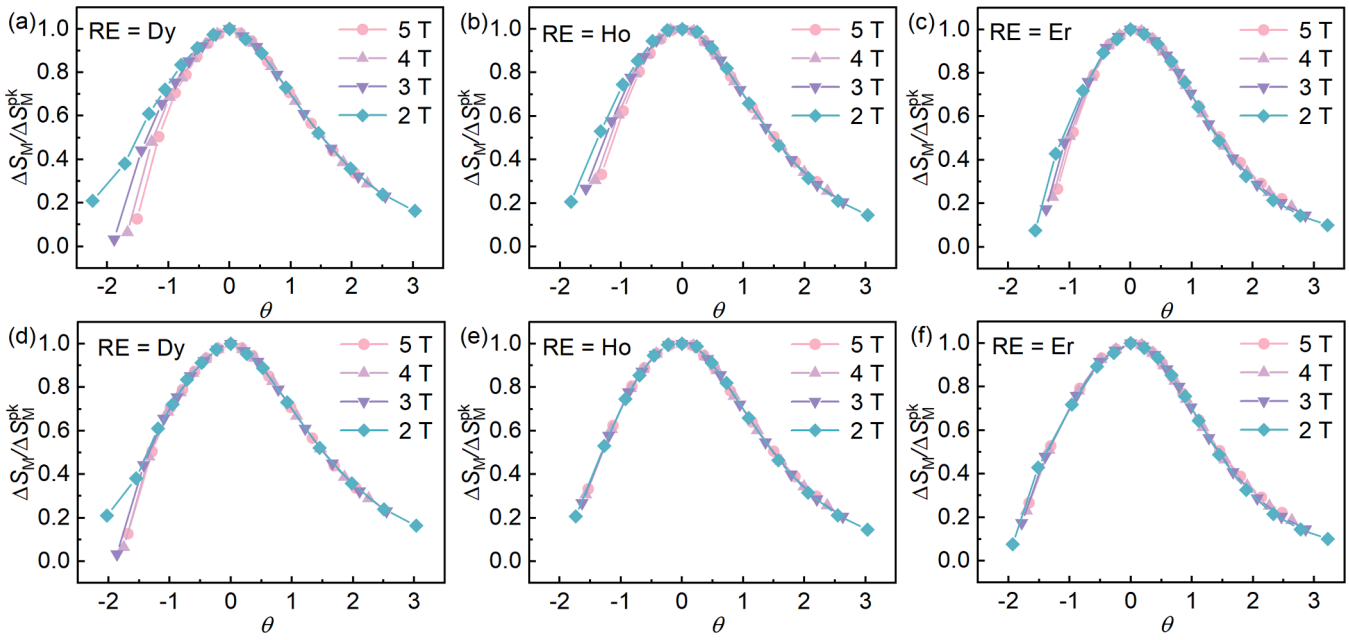

Fig. 10. The universal curves of $Gd_{36}RE_{20}Ni_{20}Al_{24}$ alloys with RE = (a) Dy, (b) Ho, and (c) Er at $\mu_0\Delta H$ = 2–5 T using one reference temperature, and (d) Dy, (e) Ho, and (f) Er using two reference temperatures.

alloy, which collapse well onto a single curve, the other curves exhibit deviations in the range of $\theta < -0.5$. The deviations associated with the identification of the phase transition type are evaluated according to the following equation [41], Dispersion = $100 \times \frac{W\,(\theta=-1.5)}{\text{Average } \Delta S_M/\Delta S_M^{pk}(\theta=-1.5)}$, where W is the vertical spreading of each universal curve. The dispersions for one-reference-temperature universal curves of $Gd_{36}RE_{20}Ni_{20}Al_{24}$ (RE = Dy, Ho) alloys are 125.98 % and 32.26 %, respectively. A dispersion value of 100 % is commonly regarded as the criterion distinguishing SOMT materials [41]. Therefore, $Gd_{36}RE_{20}Ni_{20}Al_{24}$ (RE = Ho, Er) alloys exhibit SOMT across the tested temperature range, whereas $Gd_{36}Dy_{20}Ni_{20}Al_{24}$ displays FOMT at low temperatures.

There is a power law relationship between $|\Delta S_M^{pk}|$ and $\mu_0\Delta H$, i.e., $|\Delta S_M^{pk}| = a(\mu_0\Delta H)^b$, where a and b are coefficients. Fig. 11(a) illustrates the magnetic field dependence of $|\Delta S_M^{pk}|$ for $Gd_{36}RE_{20}Ni_{20}Al_{24}$ (RE = Dy, Ho, Er) alloys, together with the corresponding power-law fits. The fitted a and b are 1.765 ± 0.015 and 0.928 ± 0.012 for RE = Dy; 1.915 ± 0.017 and 0.949 ± 0.013 for RE = Ho; and 1.882 ± 0.012 and 0.944 ± 0.012 for RE = Er. The larger exponent b compared with the mean-field theoretical prediction (2/3) is attributed to a distribution of T_C [50], which originates from local inhomogeneities, i.e., chemical short-range order in these alloys [51].

The relationship between $|\Delta S_M|$ and $\mu_0\Delta H$ is generally assumed as $|\Delta S_M| \propto (\mu_0\Delta H)^n$ [49]. Since exponent n depends on both the magnetic field change and temperature, its local value can be determined using the following equation:

$$n = \mathrm{d}\ln|\Delta S_M|/\mathrm{d}\ln|\mu_0\Delta H| \quad (7)$$

Fig. 11(b) shows the n-T curves for the studied alloys at $\mu_0\Delta H$ = 5 T All curves exhibit a minimum near the T_C, while at both low and high temperatures the exponent n does not reach the expected limiting values (≈1 for the ferromagnetic state at low temperatures and ≈2 for the paramagnetic state at high temperatures). The deviation from the expected tendency toward 1 at low temperatures arises from the SG state caused by RMA. At high temperatures, exponent n exhibits a monotonically increasing trend with rising temperature, which may be due to the measurement range not extending to the temperatures where n approaches 2. Such behavior has also been reported in other RE-based amorphous alloys [52]. The n-T curves for all alloys remain below 2

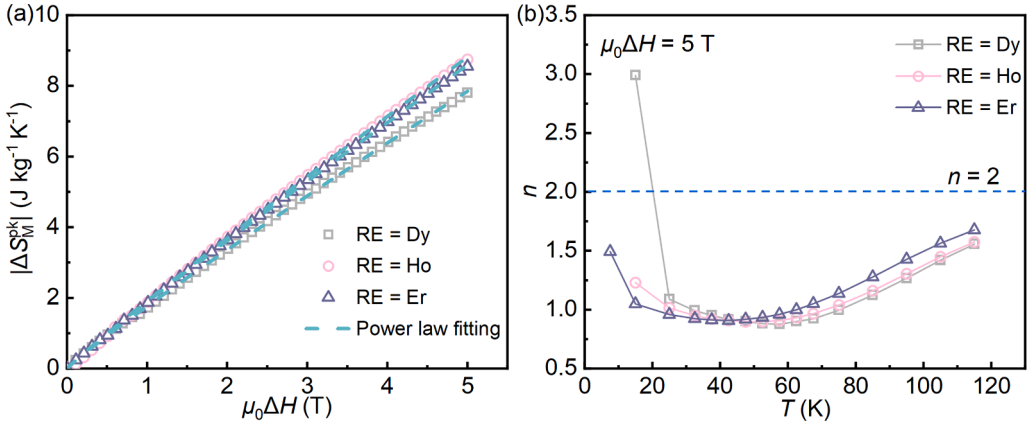

Fig. 11. (a) The $\mu_0\Delta H$ dependence of $|\Delta S_M^{pk}|$ and (b) n-T curves at $\mu_0\Delta H$ = 5 T for $Gd_{36}RE_{20}Ni_{20}Al_{24}$ (RE = Dy, Ho, Er) alloys. The dashed lines in (a) represent the fitting curves.

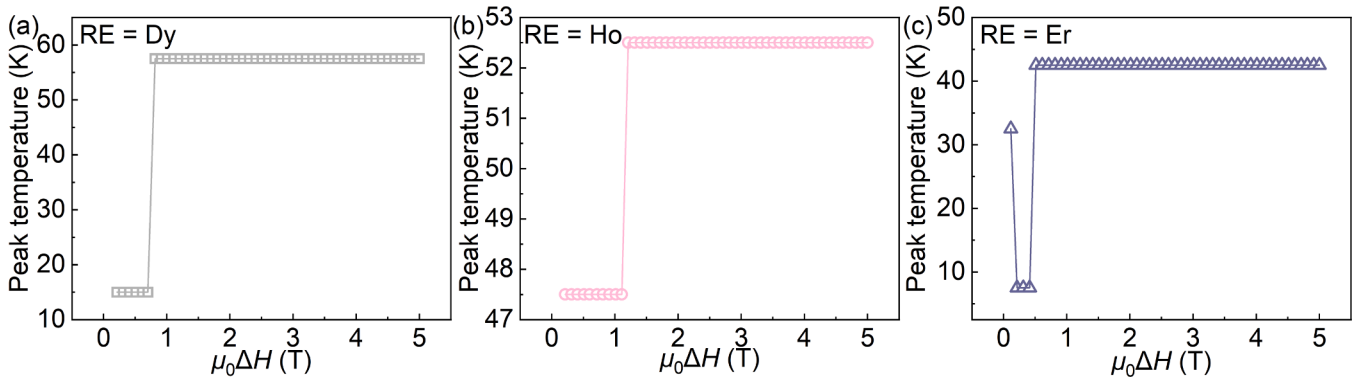

Fig. 12. Peak temperatures corresponding to $|\Delta S_M^{pk}|$ as a function of the $\mu_0\Delta H$ for $Gd_{36}RE_{20}Ni_{20}Al_{24}$ alloys with RE = (a) Dy, (b) Ho, and (c) Er.

throughout the entire temperature range, except for $Gd_{36}Dy_{20}Ni_{20}Al_{24}$, which shows $n > 2$ at low temperatures. These results indicate that, except for $Gd_{36}Dy_{20}Ni_{20}Al_{24}$, which exhibits FOMT at low temperatures, the other alloys display SOMT across the tested temperature range [47, 53]. This finding is consistent with the analyses of the universal curves and Arrott plots. The FOMT observed in $Gd_{36}Dy_{20}Ni_{20}Al_{24}$ alloy is ascribed to its SG state [34,35]. The peak temperatures of the $|\Delta S_M|$-T curves for $Gd_{36}RE_{20}Ni_{20}Al_{24}$ (RE = Dy, Ho, and Er) are 57.5, 52.5 and 42.5 K, respectively, at $\mu_0\Delta H = 5$ T. The n values at the peak temperatures are 0.876 ± 0.041 for RE = Dy, 0.900 ± 0.041 for RE = Ho, and 0.907 ± 0.041 for RE = Er). These values are very close to the b values of the studied alloys. This is attributed to the peak temperature being constant under most $\mu_0\Delta H$, as illustrated in Fig. 12.

4. Conclusions

In summary, the $Gd_{36}RE_{20}Ni_{20}Al_{24}$ (RE = Dy, Ho, Er) alloys were prepared by melt-spinning. All the studied alloys exhibit a fully amorphous structure and a SG state. The T_C of the alloys can be tuned within 40–50 K, proportional to the de Gennes factor of the substituted rare-earth elements. All the alloys exhibit SOMT characteristics, except for $Gd_{36}Dy_{20}Ni_{20}Al_{24}$, which shows a FOMT at low temperatures, originating from its SG state. The disordered atomic structure, chemical disorder, and SG state contribute to the relatively wide working temperature spans of the studied alloys. The $|\Delta S_M^{pk}|$ values for alloys with RE = Dy, Ho and Er are 7.79, 8.75 and 8.55 J kg^{-1} K^{-1}, respectively, with corresponding RC values of 470, 528, and 492 J kg^{-1} at $\mu_0\Delta H = 5$ T. The relatively large magnetocaloric performance of these amorphous HEAs make them promising candidates for refrigerant applications in the 20–77 K temperature range relevant to hydrogen liquefaction.

Data statement

Data will be made available on request.

CRediT authorship contribution statement

Zhongwei Pei: Writing – original draft, Validation, Investigation, Formal analysis, Data curation. **Hangboce Yin:** Writing – review & editing, Supervision, Methodology, Funding acquisition, Conceptualization. **Songhao Shao:** Investigation, Formal analysis. **Yan Zhang:** Formal analysis. **Meng Gao:** Formal analysis. **Lijian Song:** Formal analysis. **Wei Xu:** Formal analysis. **Yu Tong:** Formal analysis. **Xiao Jin:** Formal analysis. **Jun Xu:** Formal analysis. **Mingliang Xiang:** Writing – review & editing, Supervision, Software, Resources, Methodology, Investigation, Formal analysis. **Jun-Qiang Wang:** Supervision, Methodology, Formal analysis. **Juntao Huo:** Supervision, Methodology, Funding acquisition, Conceptualization.

Declaration of competing interest

The authors declare that they have no known competing financial interests or personal relationships that could have appeared to influence the work reported in this paper.

Acknowledgments

We acknowledge financial support from the National Natural Science Foundation of China (Nos. 52301223, 52222105, 51922102, 52001319, 92163108, 52201193), Zhejiang Provincial Natural Science Foundation of China (Nos. LGF22E010002, LZ22A030001), "Pioneer and Leading Goose" R&D Program of Zhejiang (No. 2022C01023), Ningbo Key Scientific and Technological Project (No. 2019B10051), and Natural Science Foundation of Ningbo City (No. 2024Z075). This research was supported by Zhejiang Provincial Natural Science Foundation of China under Grant No LQ24E010004. H.Y. acknowledges the help from Dr. Yunfei Wang for valuable discussions and helpful answers to related questions.

References

[1] F.X. Long, Y.Z. Song, H.C. Li, Y.J. Xu, F.Y. Tian, Y.P. Zhang, T.Y. Li, H. Liu, J. Z. Hao, L.H. He, X.R. Xing, F.X. Hu, J. Chen, High entropy: a general strategy for broadening the operating temperature of magnetic refrigeration, J. Am. Chem. Soc. 147 (2025) 4349–4356.
[2] K.M. Qiao, Z. Cui, X.W. Hao, Q. Zhao, Y.X. Xu, D.K. Wang, J.Y. Liu, D.D. Wang, Y. G. Xia, W. Yin, J.Z. Hao, L.H. He, C. Romero-Muñiz, J.Y. Law, V. Franco, Q.Y. Ren, H. Zhang, Giant room-temperature magnetocaloric effect MM′X alloys explored by machine learning, Acta Mater. 297 (2025) 121344.
[3] L. Tian, H.B. Sun, Z.J. Mo, X.Q. Gao, Z.X. Li, G.D. Liu, J. Shen, Enhanced magnetocaloric effect in rare-earth aluminum-based magnetic materials for hydrogen liquefaction, Int. J. Hydrog. Energy 98 (2025) 1205–1211.
[4] Y.F. Wang, T.F. Feng, Y.L. Li, H.J. Wei, M.H. Phan, F.X. Qin, Designing the magnetocaloric tunability by driving ferromagnetic and antiferromagnetic interactions in Gd-based microwires, J. Magn. Magn. Mater. 624 (2025) 173031.
[5] J.Y. Law, V. Franco, Review on magnetocaloric high-entropy alloys: design and analysis methods, J. Mater. Res. 38 (2023) 37–51.
[6] J.Z. Hao, B.J. Wang, F.X. Hu, J. Wang, J.T. Wang, H.B. Zhou, F.R. Shen, F.X. Liang, Z.B. Yu, Y.H. Gao, J.Y. Law, V. Franco, L.H. He, J. He, D. Liu, J.R. Sun, B.G. Shen, Competitive driving effect on calorics by dual-fields in ferroic materials with strong magnetostructural coupling, Acta Mater. 265 (2024) 119596.
[7] W. Liu, T. Gottschall, F. Scheibel, E. Bykov, N. Fortunato, A. Aubert, H.B. Zhang, K. Skokov, O. Gutfleisch, Designing magnetocaloric materials for hydrogen liquefaction with light rare-earth laves phases, J. Phys. Energy 5 (2023) 034001.
[8] A. Ahmad, E. Oko, A. Ibhadon, Comparative energy and exergy analysis of ortho-para hydrogen and non-ortho-para hydrogen conversion in hydrogen liquefaction, Int. J. Hydrog. Energy 78 (2024) 991–1003.
[9] Q. Cao, Z.P. Wang, M. Wang, Y.J. Chen, P.C. Wang, L.C. Ge, P. Li, Q.Y. Zhao, B. Wang, Z.H. Gan, Improving hydrogen liquefaction efficiency based on the temperature-distributed refrigeration method in regenerative refrigerators, Int. J. Hydrog. Energy 57 (2024) 540–548.
[10] M. Aziz, Liquid hydrogen: a review on liquefaction, storage, transportation, and safety, Energies 14 (2021) 5917.
[11] J. Bian, X.W. Zhang, R. Zhang, W.H. Cai, Y.H. Hua, X.W. Cao, Conceptual design and analysis of a new hydrogen liquefaction process based on heat pump systems, Appl. Energy 374 (2024) 124020.

[12] J.T. Huo, L.S. Huo, H. Men, X.M. Wang, A. Inoue, J.Q. Wang, C.T. Chang, R.W. Li, The magnetocaloric effect of Gd-Tb-Dy-Al-M (M = Fe, Co and Ni) high-entropy bulk metallic glasses, Intermetallics 58 (2015) 31–35.
[13] X. Wang, Q. Wang, B. Tang, P. Yu, L. Xia, D. Ding, Large magnetic entropy change and adiabatic temperature rise of a ternary $Gd_{34}Ni_{33}Al_{33}$ metallic glass, J. Rare Earths 39 (2021) 998–1002.
[14] Y.S. Ma, H.B.C. Yin, F. Chen, M. Gao, L.J. Song, Y. Zhang, W. Xu, L.M. Wang, J. T. Huo, S.Z. Zhang, J.Q. Wang, Magnetocaloric effect in $(Tm_{67}Cu_{33})_{80}Al_{20}$ amorphous alloy, J. Non Cryst. Solids 604 (2023) 122151.
[15] L. Xue, L.L. Shao, B.S. Zhang, Z.Z. Li, J.B. Cheng, B.L. Shen, Magnetic behaviors and magnetocaloric effects in rare earth high-entropy amorphous/nanocrystalline alloys, J. Rare Earths 42 (2024) 129–136.
[16] S.J. Wei, H.X. Shen, L.Y. Zhang, F.Y. Cao, J.F. Sun, Magnetic properties and magnetocaloric effects of rare-earth based high-entropy amorphous microwires, J. Mater. Res. Technol. 33 (2024) 6216–6222.
[17] S.J. Wei, H.X. Shen, L.Y. Zhang, L. Luo, X.X. Tang, J.F. Sun, X.Q. Li, Microstructure and magnetocaloric properties of melt-extracted SmGdDyCoAl high-entropy amorphous microwires, Rare Metals 43 (2023) 1234–1242.
[18] V. Franco, J.S. Blázquez, J.J. Ipus, J.Y. Law, L.M. Moreno-Ramírez, A. Conde, Magnetocaloric effect: from materials research to refrigeration devices, Prog. Mater. Sci 93 (2018) 112–232.
[19] G. Lei, M. Huai Jin, W. Peng Yu, C. Juan, Z. Ying De, Y. Hui Qin, G. Fei, Z. Peng Chao, S. Boyu, H. Jiao Hong, J. Xiang, Cryogenic temperature magnetocaloric effect and critical behavior of GdDyErAlM (M=Fe, Co, Ni) high entropy amorphous alloys, J. Mater. Res. Technol. 32 (2024) 1493–1508.
[20] J.B. Jia, Y.S. Du, X.F. Wu, X.Q. Gao, L. Ma, G. Cheng, J. Wang, J.T. Zhao, G.H. Rao, Magnetic properties and large magnetocaloric effect in the amorphous RE_2Co (RE = Tb, Dy, Er) ribbons, J. Magn. Magn. Mater. 615 (2025) 172779.
[21] A. Elouafi, S. Ezairi, F. Lmai, A. Tizliouine, Excellent magnetocaloric effect at cryogenic temperature in amorphous ($Fe_{35}RE_{65}$) (RE = Er, Dy and Gd) alloys, J. Magn. Magn. Mater. 588 (2023) 171381.
[22] H.B.C. Yin, J.Y. Law, Y.J. Huang, V. Franco, H.X. Shen, S.D. Jiang, Y. Bao, J.F. Sun, Design of Fe-containing GdTbCoAl high-entropy-metallic-glass composite microwires with tunable Curie temperatures and enhanced cooling efficiency, Mater. Des. 206 (2021) 109824.
[23] H.B.C. Yin, J.Q. Wang, Y.J. Huang, H.X. Shen, S. Guo, H.B. Fan, J.T. Huo, J.F. Sun, Relating microstructure to magnetocaloric properties in $RE_{36}Tb_{20}Co_{20}Al_{24}$ (RE = Gd, Dy or Ho) high-entropy metallic-glass microwires designed by binary eutectic clusters method, J. Mater. Sci. Technol. 149 (2023) 167–176.
[24] H.W. Luan, K.R. Li, L.X. Shi, W. Zhao, H.T. Bu, P. Gong, K.F. Yao, Recent progress in high-entropy metallic glasses, J. Mater. Sci. Technol. 161 (2023) 50–62.
[25] L. Xue, L.L. Shao, Q. Luo, B.L. Shen, $Gd_{25}RE_{25}Co_{25}Al_{25}$ (RE = Tb, Dy and Ho) high-entropy glassy alloys with distinct spin-glass behavior and good magnetocaloric effect, J. Alloys Compd. 790 (2019) 633–639.
[26] D. Turnbull, Under what conditions can a glass be formed? Contemp. Phys. 10 (1969) 473–488.
[27] Z.P. Lu, Y. Li, S.C. Ng, Reduced glass transition temperature and glass forming ability of bulk glass forming alloys, J. Non Cryst. Solids 270 (2000) 103–114.
[28] Z.P. Lu, C.T. Liu, A new glass-forming ability criterion for bulk metallic glasses, Acta Mater. 50 (2002) 3501–3512.
[29] T. Zhang, A. Inoue, T. Masumoto, Amorphous Zr-AI-TM (TM =Co, Ni, Cu) alloys with significant supercooled liquid region of over 100 K, Mater. Trans. JIM 32 (1991) 1005–1010.
[30] A. Inoue, H. Koshiba, T. Zhang, A. Makino, Wide supercooled liquid region and soft magnetic properties of $Fe_{56}Co_7Ni_7Zr_{0-10}Nb$ (or Ta)$_{0-10}B_{20}$ amorphous alloys, J. Appl. Phys. 83 (1998) 1967–1974.
[31] L. Deng, A. Gebert, L. Zhang, H.Y. Chen, D.D. Gu, U. Kühn, M. Zimmermann, K. Kosiba, S. Pauly, Mechanical performance and corrosion behaviour of Zr-based bulk metallic glass produced by selective laser melting, Mater. Des. 189 (2020) 108532.
[32] K.A. Gschneidner, A.O. Pecharsky, V.K. Pecharsky, Low Temperature Cryocooler Regenerator Materials, Springer US, Boston, MA, 2003, pp. 457–465.
[33] J.T. Huo, L.S. Huo, J.W. Li, H. Men, X.M. Wang, A. Inoue, C.T. Chang, J.Q. Wang, R.W. Li, High-entropy bulk metallic glasses as promising magnetic refrigerants, J. Appl. Phys. 117 (2015) 073902.
[34] F. Yuan, J. Du, B.L. Shen, Controllable spin-glass behavior and large magnetocaloric effect in Gd-Ni-Al bulk metallic glasses, Appl. Phys. Lett. 101 (2012) 032405.
[35] J. Li, L. Xue, W.M. Yang, C.C. Yuan, J.T. Huo, B.L. Shen, Distinct spin glass behavior and excellent magnetocaloric effect in $Er_{20}Dy_{20}Co_{20}Al_{20}RE_{20}$ (RE = Gd, Tb and Tm) high-entropy bulk metallic glasses, Intermetallics 96 (2018) 90–93.
[36] K. Binder, A.P. Young, Spin glasses: experimental facts, theoretical concepts, and open questions, Rev. Mod. Phys. 58 (1986) 801–976.
[37] C. Jayaprakash, S. Kirkpatrick, Random anisotropy models in the Ising limit, Phys. Rev. B 21 (1980) 4072.
[38] J. Du, Q. Zheng, E. Brück, K.H.J. Buschow, W.B. Cui, W.J. Feng, Z.D. Zhang, Spin-glass behavior and magnetocaloric effect in Tb-based bulk metallic glass, J. Magn. Magn. Mater. 321 (2009) 413–417.
[39] Q. Luo, B. Schwarz, N. Mattern, J. Eckert, Giant irreversible positive to large reversible negative magnetic entropy change evolution in Tb-based bulk metallic glass, Phys. Rev. B 82 (2010) 024204.
[40] B.K. Banerjee, On a generalised approach to first and second order magnetic transitions, Phys. Lett. 12 (1964) 16–17.
[41] C.M. Bonilla, J. Herrero-Albillos, F. Bartolomé, L.M. García, M. Parra-Borderías, V. Franco, Universal behavior for magnetic entropy change in magnetocaloric materials: an analysis on the nature of phase transitions, Phys. Rev. B 81 (2010) 224424.
[42] Q. Luo, W.H. Wang, Magnetocaloric effect in rare earth-based bulk metallic glasses, J. Alloys Compd. 495 (2010) 209–216.
[43] M.E. Wood, W.H. Potter, General analysis of magnetic refrigeration and its optimization using a new concept: maximization of refrigerant capacity, Cryogenics 25 (1985) 667–683.
[44] J.T. Huo, J.Q. Wang, W.H. Wang, Denary high entropy metallic glass with large magnetocaloric effect, J. Alloys Compd. 776 (2019) 202–206.
[45] X.C. Zhong, X.W. Huang, X.Y. Shen, H.Y. Mo, Z.W. Liu, Thermal stability, magnetic properties and large refrigerant capacity of ternary $Gd_{55}Co_{35}M_{10}$ (M = Mn, Fe and Ni) amorphous alloys, J. Alloys Compd 682 (2016) 476–480.
[46] J.W. Yeh, Recent progress in high-entropy alloys, Eur. J. Control 31 (2006) 633–648.
[47] V. Franco, J.S. Blázquez, A. Conde, Field dependence of the magnetocaloric effect in materials with a second order phase transition: a master curve for the magnetic entropy change, Appl. Phys. Lett. 89 (2006) 222512.
[48] J.Y. Law, L.M. Moreno-Ramírez, Á. Díaz-García, A. Martín-Cid, S. Kobayashi, S. Kawaguchi, T. Nakamura, V. Franco, MnFeNiGeSi high-entropy alloy with large magnetocaloric effect, J. Alloys Compd. 855 (2021) 157424.
[49] V. Franco, A. Conde, Scaling laws for the magnetocaloric effect in second order phase transitions: from physics to applications for the characterization of materials, Int. J. Refrig. 33 (2010) 465–473.
[50] V. Franco, A. Conde, V. Provenzano, R.D. Shull, Scaling analysis of the magnetocaloric effect in $Gd_5Si_2Ge_{1.9}X_{0.1}$ (X=Al, Cu, Ga, Mn, Fe, Co), J. Magn. Magn. Mater. 322 (2010) 218–223.
[51] X.M. Huang, X.D. Wang, Y. He, Q.P. Cao, J.Z. Jiang, Are there two glass transitions in Fe–M–Y–B (M=Mo, W, Nb) bulk metallic glasses? Scr. Mater. 60 (2009) 152–155.
[52] L.L. Shao, Q. Luo, M.J. Zhang, L. Xue, J.X. Cui, Q.Z. Yang, H.B. Ke, Y. Zhang, B. L. Shen, W.H. Wang, Dual-phase nano-glass-hydrides overcome the strength-ductility trade-off and magnetocaloric bottlenecks of rare earth based amorphous alloys, Nat. Commun. 15 (2024) 4159.
[53] J.Y. Law, V. Franco, L.M. Moreno-Ramírez, A. Conde, D.Y. Karpenkov, I. Radulov, K.P. Skokov, O. Gutfleisch, A quantitative criterion for determining the order of magnetic phase transitions using the magnetocaloric effect, Nat. Commun. 9 (2018) 2680.